Journal of Photochemistry and Photobiology A: Chemistry 216 (2010) 119–125

Contents lists available at ScienceDirect

Journal of Photochemistry and Photobiology A: Chemistry

journal homepage: www.elsevier.com/locate/jphotochem

Photoelectrochemical water splitting at nanostructured $ZnFe_2O_4$ electrodes

Asif Ali Tahir, K.G. Upul Wijayantha*

Department of Chemistry, Loughborough University, Loughborough, Leics, LE 11 3TU, UK

ARTICLE INFO

Article history:
Available online 6 August 2010

Keywords:
$ZnFe_2O_4$
Ferrite
Nanostructure
Photoelectrochemical
Water splitting
AACVD

ABSTRACT

Semiconducting nanocrystalline $ZnFe_2O_4$ thin films were deposited by aerosol-assisted chemical vapour deposition (AACVD) for photoelectrochemical (PEC) water splitting. The effect of deposition parameters such as solvent type, temperature and deposition time on PEC properties has been investigated. The SEM analysis illustrated that the morphology of the films changes significantly with the change of solvent. The films deposited from ethanolic precursor solution have a morphology consisting of interconnected cactus-like $ZnFe_2O_4$ structure growing vertically from the FTO substrate. The current–voltage characterization proved that the nanocrystalline $ZnFe_2O_4$ electrodes exhibit *n*-type semiconducting behaviour and the photocurrent was found strongly dependent on the deposition solvent, deposition temperature and deposition time. The maximum photocurrent density of 350 $\mu A/cm^2$ at 0.23 V vs. Ag/AgCl/3 M KCl (~1.23 V vs. RHE) was obtained for the $ZnFe_2O_4$ electrode synthesized using the optimum deposition temperature of 450 °C, the deposition time of 35 min, and 0.1 M solution of (**1**) in ethanol. The electrode gave an incident photon to electron conversion efficiency of 13.5% at an applied potential of 0.23 V vs. Ag/AgCl/3 M KCl at 350 nm. The donor density of the $ZnFe_2O_4$ was 3.24×10^{24} m^{-3} and the flatband potential is approximately −0.17 V, which remarkably agrees with the photocurrent onset potential of −0.18 V vs. Ag/AgCl/3 M KCl.

1. Introduction

Hydrogen is a potential fuel with desirable properties. Its energy storage capacity is 120,000 J/g as compared to 40,000 for oil and 30,000 for coal [1]. Furthermore, hydrogen has the advantage over conventional fossil or nuclear energy sources in that combustion in a thermal engine or fuel cell does not result in pollution of the environment.

Hydrogen production by water splitting has been a goal of semiconductor photoelectrochemistry for nearly four decades. The concept is based on the photosynthetic cell. The photosynthetic cell operates on the principle that there are two redox systems in the electrolyte and upon light absorption and generation of electron and hole pairs in the semiconductor photoanode (photocathode): one redox system reacts with the photogenerated holes (electrons) at the surface of the semiconductor photoanode (photocathode) and the other reacts with the electrons (holes) entering at the counter electrode. For photoelectrochemical (PEC) water splitting cells the overall reaction is the cleavage of water by sunlight. Using a titanium dioxide electrode as the photoanode in a (PEC) cell, Fujishima and Honda demonstrated water photolysis for the first time in 1972 [2]. Having a band gap of 3–3.2 eV, TiO_2 absorbs only 4% of the AM 1.5 solar spectrum. Therefore, TiO_2 is not the ideal choice for the photoelectrode material in water photolysis although its conduction band energy is favourable.

The energy difference between the oxygen evolution potential and the hydrogen evolution potential is 1.229 eV at 25 °C. Therefore, ideally one would like to have a chemically and optically stable semiconductor, in which the conduction and valence bands are positioned favourably so that they straddle the hydrogen and oxygen evolution potentials. To overcome the overpotential which is mainly associated with oxygen evolution, a semiconductor material with a band gap of 1.8–2.0 eV is preferred. Furthermore, the semiconductor material should be stable for prolonged exposure to sunlight, resistive for undesirable processes such as dissolution and photocorrosion, and economical for mass production [3,4]. Considerable efforts have been made to extend the spectral response of semiconductors such as TiO_2 towards the visible region or to develop alternative semiconductors such as $SrTiO_3$ [5], $BiVO_4$ [6] and α-Fe_2O_3 [7]. However, extensive work on finding a prospective semiconductor that meets all above-mentioned criteria has been so far unsuccessful. Recently, we have studied the PEC properties of a number of anodic semiconductor materials such as WO_3 [1], α-Fe_2O_3 [8], $NiTiO_3$ [9] with the aim of employing them in solar water splitting devices.

Among *n*-type semiconductor materials, α-Fe_2O_3, is a potential candidate with ~2.2 eV band gap that is sufficiently large enough for water splitting but small enough to collect a sufficient fraction

* Corresponding author. Tel.: +44 01509 222574; fax: +44 01509 223925.
E-mail address: U.Wijayantha@lboro.ac.uk (K.G.U. Wijayantha).

1010-6030/$ – see front matter © 2010 Elsevier B.V. All rights reserved.
doi:10.1016/j.jphotochem.2010.07.032

of sunlight, ~40% energy [7,8,10]. The current work on α-Fe_2O_3 is focused on modelling and designing of hematite with appropriate morphology, size, shape and texture in order to probe, tune and optimize the PEC properties. Although adding various dopants (Si, Pt, Zn and Ti) to α-Fe_2O_3 structure has been a popular strategy to enhance the photocurrent performance, the exact doping mechanism, role of dopants and doping level are still a subject of discussion [11,12]. The majority of dopants have been shown to decrease the photocurrent efficiency [12] and the efforts to fabricate best efficient α-Fe_2O_3 based photoanodes are still ongoing. Therefore, along with the α-Fe_2O_3 there is an urgent need of exploring new materials for a better light to chemical conversion efficiencies.

$ZnFe_2O_4$ has attracted attention in photoelectric conversion and photochemical hydrogen production from water due to its visible light sensitivity and good photochemical stability [13,14]. Recently, it has been reported that $ZnFe_2O_4/TiO_2$ nanocomposite is a photocatalyst which is more effective than widely studied TiO_2 based nanomaterials [15,16]. An enhanced photocurrent has been demonstrated for double-layered films composed of $ZnFe_2O_4$ and TiO_2 [17]. In one of our previous works, we reported a detailed account on the deposition of nanostructured $ZnFe_2O_4$ thin films from single source precursor and structural and optical properties of the deposited thin films [18]. In this article we report the photoelectrochemical properties of $ZnFe_2O_4$ thin films and effect of deposition parameters such as deposition solvent, temperature and time on PEC properties. Although there are a few reports on the photocatalytic and photoelectrochemical properties of $ZnFe_2O_4/TiO_2$ nanocomposite, to our knowledge $ZnFe_2O_4$ has not been studied for the PEC water splitting on its own to date. Thin films are further characterized by X-ray photoelectron spectroscopy, Raman spectroscopy and scanning electron microscopy in this work.

2. Experimental

$ZnFe_2O_4$ thin films were deposited on fluorine-doped tin oxide (FTO) (TEC 8 Pilkington, 8 Ω/sq) substrate by aerosol-assisted chemical vapour deposition (AACVD) using a single source heterobimetallic precursor $[Fe_2(acac)_4(dmaeH)_2][ZnCl_4]$ (**1**) (acac = 2,4-pentanedionate, dmaeH = N,N-dimethylaminoethanol) as reported elsewhere [18]. The morphology, thickness and nanostructure of thin films were controlled by altering deposition solvent, temperature as well as deposition time. Surface morphology of thin films was studied using a field-emission gun scanning electron microscope (Leo 1530 VP) at an accelerating voltage of 5 kV, and a working distance of 6 mm. XPS spectra were recorded using a VG Scientific Escalab Mk I instrument operating with an unmonochromatised Al Kα X-ray source (1486.6 eV). Raman spectroscopy was carried out using a HORIBA Jobin Yvon LabRAM HR (with 632.8 nm He–Ne laser) Raman Spectrophotometer. The spectrum was recorded in the range from 100–1000 cm^{-1}.

An electrochemical cell in three-electrode configuration, fitted with a quartz window, was used for photoelectrochemical characterization. All measurements were carried out in 1 M NaOH (pH 13.6) electrolyte, Ag/AgCl/3 M KCl as the reference electrode, and a platinum wire as the counter electrode. The potential of the $ZnFe_2O_4$ working electrode was controlled by a potentiostat (micro-Autolab, type III). The illumination source was an AM1.5 class A solar simulator (Solar Light 16S – 300 solar simulator). In the electrochemical cell, light enters through a quartz window and travels about a 5 mm path in the electrolyte before illuminating the photoelectrodes. The electrode was illuminated through the electrolyte side and the illumination area was 1 cm^2. For current–voltage characterization, the scan rate was maintained at 0.01 V/s and current density was recorded under light, while manually chopping at regular intervals to reveal the dark current simultaneously.

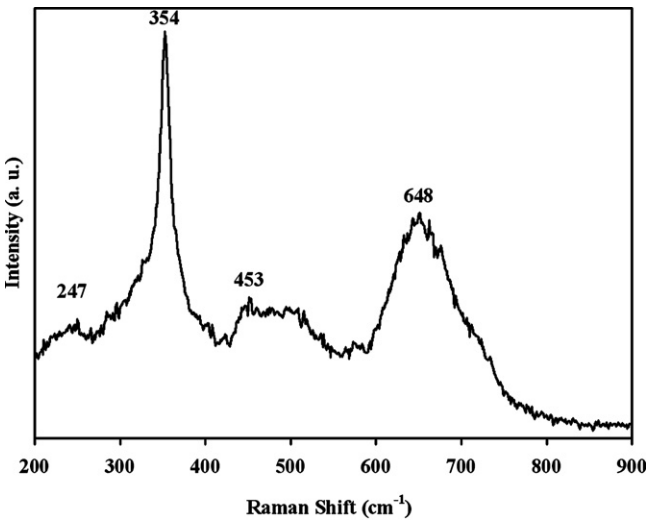

Fig. 1. Raman spectrum of an $ZnFe_2O_4$ film deposited on a FTO substrate using optimum condition of deposition temperature of 450 °C, the deposition time of 35 min, and 0.1 M solution of (**1**) in ethanol.

The incident photon to electron conversion efficiency (IPCE) was obtained by measuring the incident photons of a 75 W Xenon lamp connected to a monochromator (TMc300, Bentham Instruments Ltd.). The system was calibrated using a silicon diode. The IPCE spectra of $ZnFe_2O_4$ electrodes were measured at 0.23 V vs. Ag/AgCl/3 M KCl (~1.23 V vs. RHE) [8]. Readings were taken at every 5 nm as the monochromated light was scanned from 320 to 650 nm.

Mott–Schottky relationship was used to calculate the flat-band potential (V_{fb}) of nanostructured $ZnFe_2O_4$ thin films. The Mott–Schottky plots were constructed using capacitance data obtained from a technique based on cyclic voltammetry as described by Boschloo et al. [19] and Eggleston et al. [20].

3. Results and discussion

The nanocrystalline $ZnFe_2O_4$ thin films deposited by AACVD using precursor $[Fe_2(acac)_4(dmaeH)_2][ZnCl_4]$ (**1**) are transparent, uniform robust and adhere strongly on FTO substrate as verified by the "scotch tape test" [8,32]. The films are stable towards air atmospheric moisture and in 1 M NaOH electrolyte. Following the structural and optical characterization [18], $ZnFe_2O_4$ films were further studied by Raman and XPS spectroscopies. Thin films having different morphologies were obtained by controlling the preparation conditions. The effect of solvent, deposition temperature, and deposition time on PEC properties was investigated.

3.1. Raman spectroscopy

Raman scattering measurements were carried out for the $ZnFe_2O_4$ thin films in the range 100–1000 cm^{-1}. $ZnFe_2O_4$ has a spinel structure with space group *Fd*3*m* and has five active Raman modes ($A_{1g} + E_g + 3F_{2g}$) [21]. Fig. 1 shows that out of five Raman modes, four are observed at 247, 354, 453 and 648 cm^{-1}. It is generally accepted that the modes above 600 cm^{-1} are of A_{1g} type, involving motions of the O in tetrahedral AO_4 groups, so the mode at 648 cm^{-1} can be reasonably considered as A_{1g} symmetry. Therefore, other low frequency modes represent the characteristics of the octahedral sites (BO_6). The broad nature of first-order Raman mode at 354, 453 and 648 cm^{-1} may be due to certain amount of disorder because the Zn and Fe cations occur in the tetrahedral and

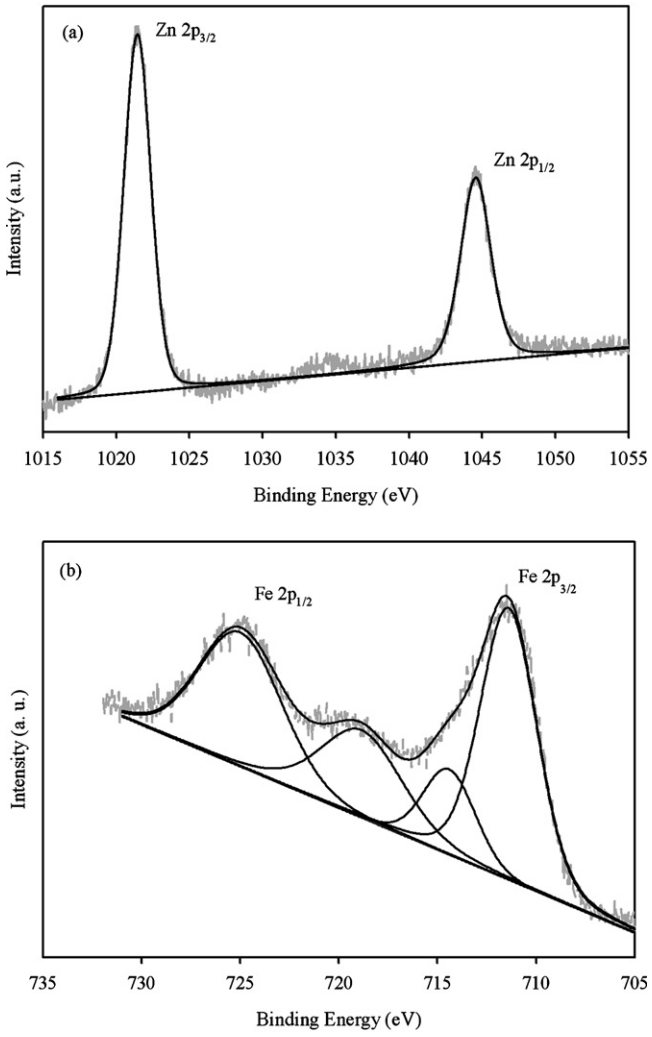

Fig. 2. Zn 2p (a) and Fe 2p (b) core-level X-ray photoelectron spectrum of the $ZnFe_2O_4$ thin films deposited using optimum condition of deposition temperature of 450 °C, the deposition time of 35 min, and 0.1 M solution of (**1**) in ethanol.

octahedral sites. Hence, the vibrations relating to these two types of cations at the same site may display two separated first-order Raman modes. If the two modes have very close vibrational frequencies, an overlapped broad peak with their average value should be observed. In this slightly inverted $ZnFe_2O_4$ spinel, Zn and Fe ions distribute at the same atomic crystal site, either the tetrahedral or octahedral form, and result in the corresponding vibrations with different frequencies. Since these two vibrations have very close wavelengths, three broad first-order Raman spectroscopic peaks were observed for $ZnFe_2O_4$ spinel [22].

3.2. X-ray photoelectron spectroscopy

In $ZnFe_2O_4$, Fe and Zn atoms exist in the lattice with more than one chemical states (A-sites or B-sites), bringing about several different contributions with different binding energies in the XPS spectra [23]. Therefore, X-ray photoelectron spectroscopy was used to reveal the surface chemical compositions of nanocrystalline $ZnFe_2O_4$ thin films. As shown in the spectrum in Fig. 2a, the peaks of 1021.4 and 1045.2 eV can be attributed to Zn $2p_{3/2}$ and $2p_{1/2}$, respectively. This reveals the oxidation state of Zn^{2+} in the sample [24,25]. The peak at 1021.4 is ascribed to the formation of zinc ferrite with the zinc atom occupying tetrahedral site. Druska et al. [26] have reported the binding energy of Zn $2p_{3/2}$ to be around 1023.0 eV in $ZnTiO_3$ where zinc occupies the octahedral site. Hence we assume that the Zn^{2+} ions occupy only tetrahedral sites. The peak at 1021.4 eV is also consistent with the XPS recorded for the standard $ZnFe_2O_4$ material [27]. Fig. 2b shows the Fe 2p peaks at binding energies of 711.4 and 725.0 eV, with a shakeup satellite at 718.8 eV, which is consistent with that reported for Fe^{3+} in $ZnFe_2O_4$ [28]. In case of zinc ferrite, the system does not contain any Fe^{2+}, so the binding energy was increased to 711.4 eV in comparison to Fe_3O_4. Though hematite and zinc ferrite contain Fe^{3+} type iron only, a slight increase in binding energy in zinc ferrite (711.4 eV) compared to that of Fe_2O_3 (711.2 eV) may be due to the change of oxygen environment of Fe in Zn ferrite. The Fe^{2+} and Fe^{3+} photoelectron peaks are always associated with satellite peaks around 6 and 8.5 eV, respectively, which are higher than the principal peak [29]. In Fe_3O_4, the satellite peak associated with $2p_{3/2}$ of Fe is not seen or it may be apparently absent because of the superposition of the two satellites. The XPS analysis also confirms that the ratio of Zn to Fe in the sample is 1:2, agreeing with the formula of $ZnFe_2O_4$.

3.3. Surface morphology

Morphology and structure of the $ZnFe_2O_4$ thin films were investigated by field-emission gun scanning electron microscopy (FEGSEM). Typical SEM images of $ZnFe_2O_4$ thin films deposited using optimum condition of deposition temperature of 450 °C, the deposition time of 35 min, and the deposition solution of 0.1 M of (**1**) in methanol and ethanol are presented in Fig. 3. The results illustrate that the morphology of the films changes significantly with the change of the deposition solution. Surface morphology of the film deposited using methanol as a solvent shows a well-defined crystallite (Fig. 3a) evenly distributed with no preferred orientation. The size of the particles ranges from 150 to 200 nm and each of them has well-defined boundaries. On the other hand, films deposited using ethanol as solvent show a fine nanostructured morphology (Fig. 3b). The well-defined particles with size in the order of 25–40 nm combine together to form a plate-like structure. The cross-section of the film (Fig. 3d) reflects that the plate-like structures are sintered together to form an interconnected cactus-like structure of $ZnFe_2O_4$ growing vertically from the FTO substrate. The vertical growth of these structures makes films more porous providing access to electrolyte solution. This results in a significant increase of photoelectrochemical properties of these electrodes compared to the electrodes deposited using methanol as the solvent.

3.4. Photoelectrochemical (PEC) characterization

3.4.1. Effect of solvent

It has already been found that the addition of an organic structure-directing agent to the precursor solution may affect both the crystallinity and porosity of the resulting thin films [30]. At the outset, it is important to determine the effect of solvent on the performance of the photoelectrodes. The AACVD technique employed herein is highly sensitive to the choice of solvent. Among many other variables, the size of the aerosol droplets relies on the viscosity and boiling point of the solvent. Different solvents, such as tetrahydrofuran (THF), methanol and ethanol have been employed for the deposition of $ZnFe_2O_4$ electrodes. As shown in Fig. 4 a strong dependence of the photocurrent density on the deposition solvent was observed, and the highest photocurrent density was found when the aerosol formed from ethanolic precursor solution. The photocurrent performance suggests that ethanol facilitates the formation of fine aerosol droplets and better nanocrystals during the deposition (see Fig. 3). The formation of fine nanostructured thin films with enhanced photocurrent for the ethanol-based films

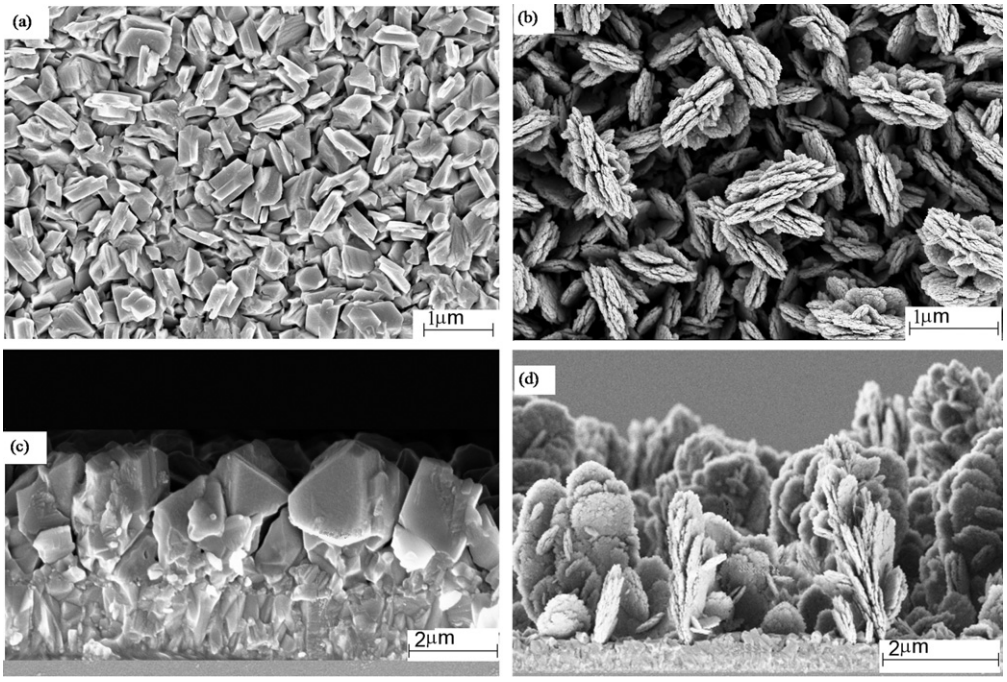

Fig. 3. SEM images of $ZnFe_2O_4$ thin films deposited on FTO substrate using optimum condition of deposition temperature of 450 °C and the deposition time of 35 min. (a) and (c) show surface morphology and cross-section for the film deposited from 0.1 M solution of (**1**) in methanol [18], whereas (b) and (d) show the same details for the film deposited from 0.1 M solution of (**1**) in ethanol.

can be explained on the basis of heat of combustion. Ethanol has much higher heat of combustion (326.68 kJ mol^{-1}) to facilitate homogeneous nucleation as compared to that of methanol (173.64 kJ mol^{-1}). Similar effect of solvent on photocurrent density has observed for thin films such as α-Fe_2O_3 by others [31]. Along with enthalpy of the system, there may be a number of other factors such as the rate of solvent evaporation, nature of bonding between precursor and solvent molecules in aerosol droplets which affect the morphology and growth of the films. All these factors may influence the homogeneous or heterogeneous nucleation by changing the enthalpy of the system. Recently, Parkin and coworkers have deposited different phases of vanadium oxides using different solvents and carrier gases and proved that the solvent and carrier gas are critical parameters in AACVD [32]. However, further studies are required to understand the effect of the solvent on the film morphology in AACVD.

3.4.2. *Effect of deposition temperature*

Along with the deposition solvent, the deposition temperature was found to be an important factor in thin film formation. The dependence of photocurrent density on substrate temperature during the AACVD deposition of $ZnFe_2O_4$ thin film is shown in Fig. 5. The photocurrent density increases with the increase of deposition temperature and reaches the optimum level at 450 °C. With further increase of the deposition temperature, the photocurrent of $ZnFe_2O_4$ electrodes decreases significantly. We believe that at low substrate temperature regime, the decomposition was not completed and as a result the nanocrystals became rich in

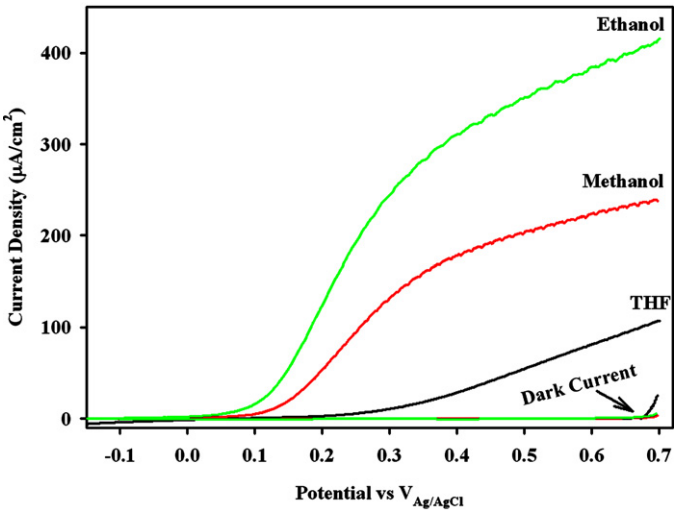

Fig. 4. Dependence of photocurrent density on deposition solvent for the $ZnFe_2O_4$ electrodes deposited at 400 °C.

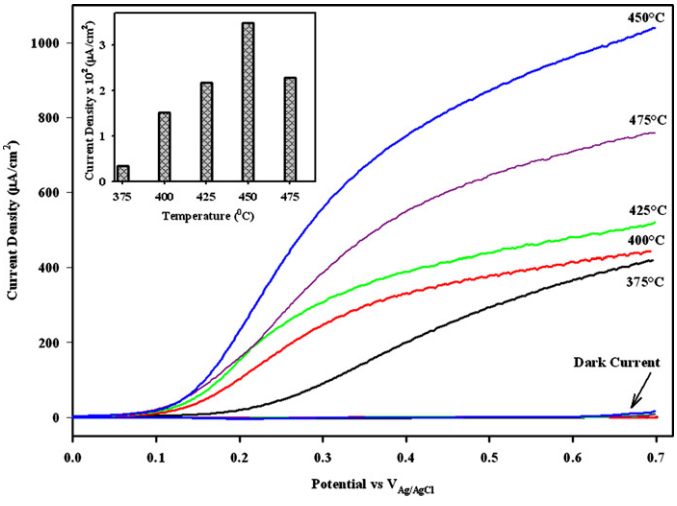

Fig. 5. *J–V* curves for $ZnFe_2O_4$ electrodes deposited using 0.1 M solution of (**1**) in ethanol for 35 min at different deposition temperatures. Inset shows the dependence of photocurrent density at 0.23 V vs. Ag/AgCl/3 M KCl on the deposition temperature.

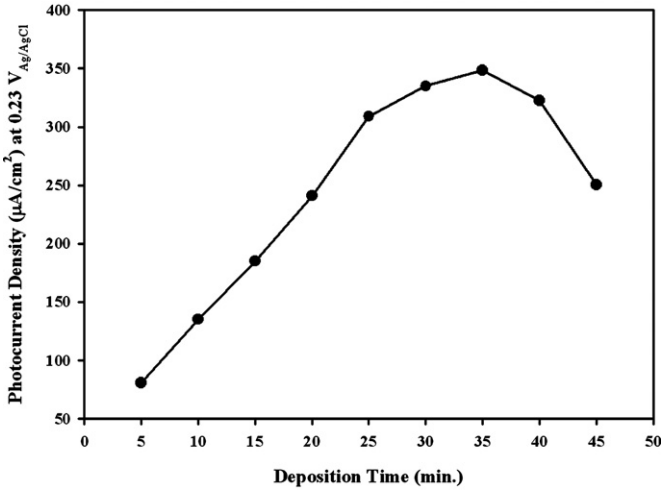

Fig. 6. Dependence of photocurrent density on the deposition time for the $ZnFe_2O_4$ electrodes deposited using optimum condition of deposition temperature of 450 °C and 0.1 M solution of (**1**) in ethanol.

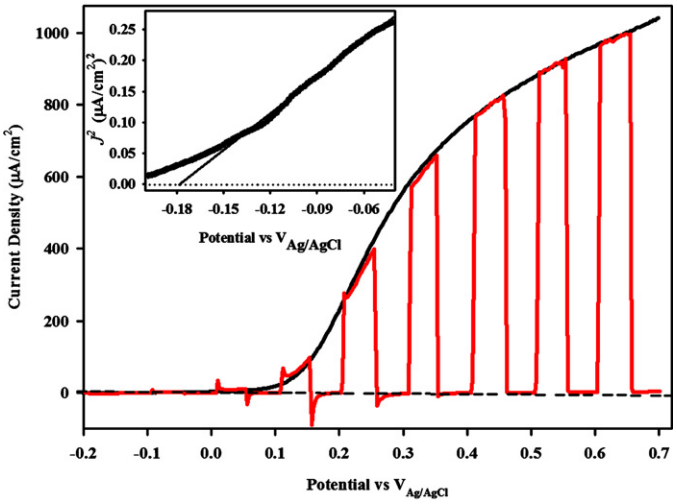

Fig. 7. Current potential curves for the nanostructured $ZnFe_2O_4$ electrodes deposited using optimum condition of deposition temperature of 450 °C, the deposition time of 35 min and 0.1 M solution of (**1**) in ethanol. The *J–V* was measured in 1 M NaOH under simulated AM1.5 sunlight at the scan rate of 0.01 V/s and light was manually chopped to obtain light and dark current simultaneously. The J^2–V plot in the inset shows photocurrent onset.

defects, leaving dislocations and kink sites. These dislocations and kink sites may act as the recombination centers for the photogenerated electron–hole pairs and consequently show a poor PEC performance. Similarly, at higher temperature regime (>450 °C) the premature decomposition and nucleation influence the film morphology and texture diminishing the photocurrent. It is reported for AACVD technique that at higher temperatures, the decomposition of the precursor starts much earlier in the gas phase and homogeneous nucleation produced powder particles before depositing on the substrate surface and resulting films have more defects and possess less adherence properties [33].

3.4.3. *Effect of deposition time*

Fig. 6 shows the dependence of photocurrent density on the electrode deposition time. As expected the electrodes corresponding to short deposition times are relatively thin whereas the electrodes associated with long deposition times are thick. The deposition time was directly correlated to the electrode thickness (data not shown). Up to 35 min, the photocurrent and deposition time (hence electrodes thickness) showed a very good correlation suggesting that photocurrent is directly related to the amount of light harvested by $ZnFe_2O_4$. The nanocrystalline electrode which showed the maximum photocurrent density had a thickness of 5 μm and corresponds to 35 min of deposition time. The observed optimum photocurrent performance could be attributed to matching the majority carrier diffusion length with the film thickness of the nanocrystalline $ZnFe_2O_4$ electrode. For electrodes with higher thickness (>5 μm, correspond to more than 35 min of deposition time) the photogenerated electrons require to travel beyond the electron diffusion length before being collected at the FTO substrate (here the electrodes were illuminated from the electrolyte side). The electron transport within fine nanocrystalline $ZnFe_2O_4$ could be significantly slow. The slow and trap dominant charge transport mechanisms within nanostructured matrix have been already reported for a number of metal oxide semiconductor systems [34,35]. Therefore, the relatively slow electron transport and associated charge recombination may be the key reasons for diminished photocurrent for electrodes that correspond to long deposition times.

Fig. 7 shows current–voltage characteristics under dark and simulated sunlight in 1 M NaOH for the $ZnFe_2O_4$ electrode deposited using optimum condition of deposition temperature of 450 °C, the deposition time of 35 min, and 0.1 M solution of (**1**) in ethanol. The photocurrent shows anodic behaviour and it was further confirmed by capacitance data (Fig. 10). The dark current is negligible up to 0.7 V vs. Ag/AgCl beyond which it is dominated by the oxygen evolution. No photocurrent saturation is observed indicating strong recombination under depletion. The sharp anodic and subsequent cathodic spikes in the photocurrent transients indicate that the recombination is relatively high in the region where the space charge layer width is narrow. The photocurrent density at 0.23 V vs. Ag/AgCl/3 M KCl is about 350 μA cm^{-2} and rises steeply up to 1.05 mA cm^{-2} as the applied voltage further increased. The photocurrent onset estimated from the J^2–*V* plot was at −0.18 V vs. Ag/AgCl/3 M KCl. The photocurrent density recorded under the steady-state conditions agrees well with its transient counterparts. Although attempts have already made to employ $ZnFe_2O_4$ as the photosensitized material for TiO_2 [17], to our knowledge there is no previous report on PEC characterization of $ZnFe_2O_4$ material itself. Furthermore, for a number of reasons we would like to distinguish this investigation from the previous work conducted to dope α-Fe_2O_3 with Zn [36,37]. Firstly, there is no evidence for the presence of Fe_2O_3 in our $ZnFe_2O_4$ electrodes [18]. Secondly, the photocurrent density achieved in the current work is significantly higher than that reported for Zn-doped α-Fe_2O_3 [36,37]. Thirdly, doping of α-Fe_2O_3 with Zn itself is a controversial area as some works claim anodic behaviour for Zn-doped α-Fe_2O_3 electrodes [10,12,36,37], whereas others argue for the cathodic properties for similar electrodes [38].

3.4.4. *Incident photon to electron conversion efficiency (IPCE) characterization*

The incident photon to electron conversion efficiency (IPCE) as a function of wavelength recorded at 0.23 V vs. Ag/AgCl/3 M KCl for the nanostructured $ZnFe_2O_4$ thin film electrodes deposited at 450 °C using 0.1 M solution of (**1**) in ethanol for 35 min is given in Fig. 8. As estimated by J^2–V characteristics, the IPCE threshold exists at about 625 nm. The maximum efficiency of 35.5% attains at 350 nm. As the wavelength is scanned from 500 to 625 nm, the IPCE gradually decreases before reaching the threshold at 625 nm. The relatively low IPCE exhibited by $ZnFe_2O_4$ electrodes could be due to the combined factors of week light absorption and high hole–electron recombination rate. Analysis of the IPCE and absorp-

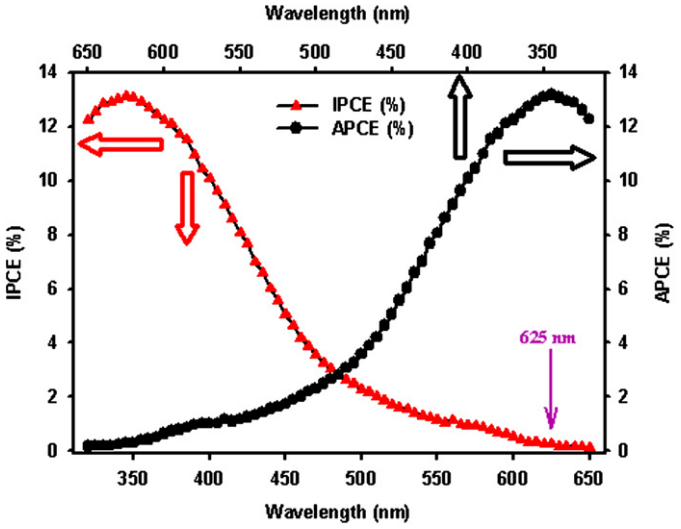

Fig. 8. IPCE and APCE spectra for the nanostructured $ZnFe_2O_4$ electrode deposited using optimum condition of deposition temperature of 450 °C, the deposition time of 35 min, and 0.1 M solution of (**1**) in ethanol.

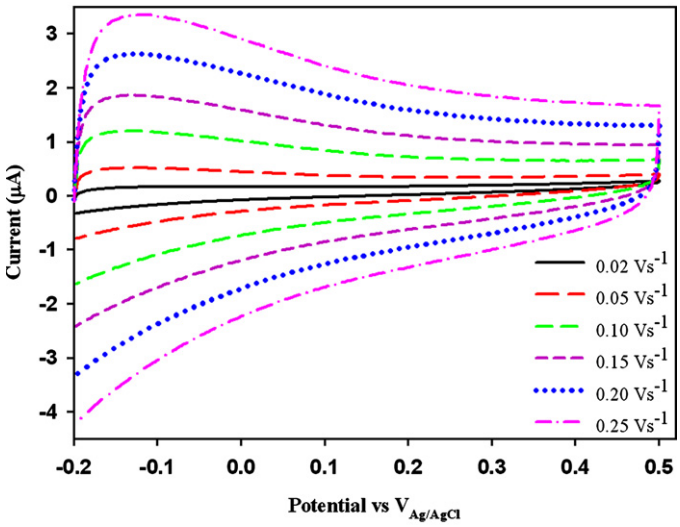

Fig. 9. Voltammograms of $ZnFe_2O_4$ electrode deposited using optimum condition of deposition temperature of 450 °C, the deposition time of 35 min, and 0.1 M solution of (**1**) in ethanol. Scan rates are 0.02, 0.05, 0.1, 0.15, 0.2 and 0.25 V s^{-1}.

tion data allows us to calculate the absorbed photon to electron conversion efficiency (APCE, internal quantum yield). The APCE spectra overlap in the entire spectral range (320–650 nm) and this overlap is consistent with the fact that the photons are absorbed in a film which mainly consists of fine branches with feature sizes comparable to the hole diffusion length.

3.5. Electrical Characterization

In cyclic voltammetry, the current is a linear function of the applied potential and in the absence of Faradaic processes, the scan-rate dependence of current can be attributed to charging and discharging of the space charge layer capacitance. Therefore in the absence of interfacial redox reactions the differential capacity (C) can be expressed as follows:

$$C = \frac{dQ}{dV} = \frac{idt}{dV} = \frac{i}{v} \quad (1)$$

where Q is the charge, V is the potential, i is the current, t is the time and v is the scan rate. The voltammograms recorded as a function of scan rate for the best $ZnFe_2O_4$ electrode are shown in Fig. 9. The current i was plotted against scan rate v at selected applied potentials (both anodic and cathodic plots were given in inset of Fig. 10). The space charge layer capacitance (C_{SC}) is measured from the slope of the line plotted at each potential. The data taken from the forward scans of the CVs are used to estimate the capacitance. The intercept of the Mott–Schottky plot (i.e. C^{-2} vs. V) was used to estimate the flatband potential (V_{fb}) as shown in Fig. 10.

The flatband potential (V_{fb}) is an important characteristic for predicting the photoelectrochemical properties. The donor density (N_D) can be calculated using the following Mott–Schottky relationship (Eq. (2)):

$$\left(\frac{1}{C}\right)^2 = 2(eN_D\varepsilon_0\varepsilon_r A^2)^{-1}\left(|V - V_{fb}| - \frac{kT}{e}\right) \quad (2)$$

where A is the surface area of the film, ε_r is the dielectric constant of $ZnFe_2O_4$ (taken as 100 [39]), ε_0 is the permittivity of free space, T is the temperature and k is the Boltzmann's constant. From the Mott–Schottky results shown in Fig. 10, the donor density of the $ZnFe_2O_4$ electrode was estimated to be 3.24×10^{24} m^{-3}, and the flatband potential is approximately −0.17 V vs. Ag/AgCl/3 M KCl. The flatband potential calculated from Fig. 10 remarkably agrees

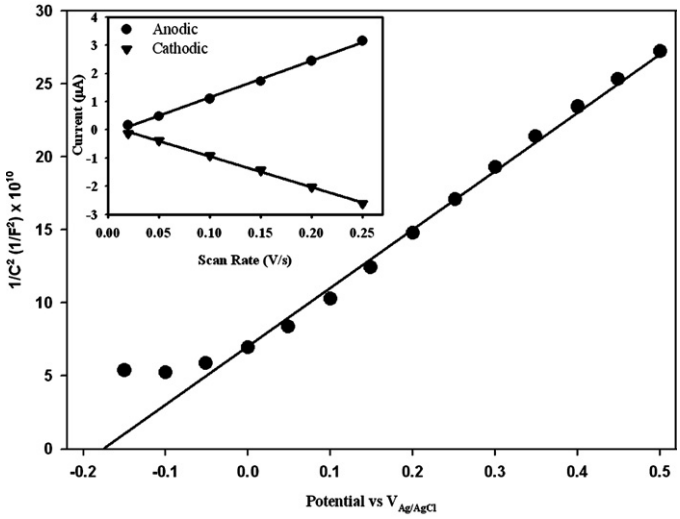

Fig. 10. Mott–Schottky plot constructed using capacitance data calculated from slope of anodic lines of current vs. scan rate at each potential. Inset: current vs. scan-rate plot demonstrates one example for both cathodic and anodic currents at −0.05 V vs. Ag/AgCl/3 M KCl.

with the photocurrent onset potential of −0.18 V vs. Ag/AgCl/3 M KCl (inset of Fig. 7).

4. Conclusion

Semiconducting nanocrystalline $ZnFe_2O_4$ thin films were deposited by aerosol assisted chemical vapour deposition (AACVD) for photoelectrochemical water splitting. Electrodes are mechanically stable and robust. An extensive study has been conducted to optimize the electrode deposition conditions and parameters. The most efficient nanocrystalline $ZnFe_2O_4$ electrode is the one prepared at a deposition temperature of 450 °C, the deposition time of 35 min, and 0.1 M solution of (**1**) in ethanol. Other deposition solvent choices resulted in electrodes that exhibited a relatively poor PEC performance, presumably due to the increase of disorder in the $ZnFe_2O_4$ films. The SEM analysis proved that the high heat of combustion of ethanol solvent promotes the vertical growth of $ZnFe_2O_4$ nanostructures from the FTO substrate making the

electrodes more porous as compared to the films deposited using methanol as the solvent. The results also showed that the long deposition time (hence the increase of electrode thickness beyond 5 μm) had a detrimental effect on the PEC performance. The maximum photocurrent density of 350 μA/cm^2 recorded at 0.23 V vs. Ag/AgCl/3 M KCl and IPCE of 13.5% at the same applied potential at 350 nm. The donor density of the $ZnFe_2O_4$ was 3.24×10^{24} m^{-3} and the flatband potential was approximately −0.17 V vs. $V_{Ag/AgCl}$, which is in excellent agreement with the photocurrent onset. The results presented in this work show that $ZnFe_2O_4$ is a promising material for photoelectrochemical water splitting and may also be a potential candidate for other solar energy applications such as photovoltaic cells and photocatalytic decomposition of organic contaminants.

Acknowledgement

This work was supported by the EPSRC award EP/F057342/1.

References

[1] K.G.U. Wijayantha, D.H. Auty, Twin cell technology for hydrogen generation, in: Encyclopaedia of Materials: Science and Technology, Elsevier, Oxford, 2008, pp. 1–5.
[2] A. Fujishima, K. Honda, Electrochemical photolysis of water at a semiconductor electrode, Nature 238 (1972) 37–38.
[3] Z. Zou, H. Arakawa, Direct water splitting into H_2 and O_2 under visible light irradiation with a new series of mixed oxide semiconductor photocatalysts, J. Photochem. Photobiol. A: Chem. 158 (2003) 145–162.
[4] M. Paulose, G.K. Mor, O.K. Varghese, K. Shankar, C.A. Grimes, Visible light photoelectrochemical and water-photoelectrolysis properties of titania nanotube arrays, J. Photochem. Photobiol. A: Chem. 178 (2006) 8–15.
[5] P. Salvador, C. Gutiíerrez, G. Campet, P. Hagenmuller, Influence of mechanical polishing on the photoelectrochemical properties of $SrTiO_3$ polycrystalline anodes, J. Electrochem. Soc. 131 (1984) 550–555.
[6] K. Sayama, A. Nomura, T. Arai, T. Sugita, R. Abe, M. Yanagida, T. Oi, Y. Iwasaki, Y. Abe, H. Sugihara, Photoelectrochemical decomposition of water into H_2 and O_2 on porous $BiVO_4$ thin-film electrodes under visible light and significant effect of Ag ion treatment, J. Phys. Chem. B 110 (2006) 11352–11360.
[7] S. Saremi-Yarahmadi, A.A. Tahir, B. Vaidhyanathan, K.G.U. Wijayantha, Fabrication of nanostructured α-Fe_2o_3 electrodes using ferrocene for solar hydrogen generation, Mater. Lett. 63 (2009) 523–526.
[8] A.A. Tahir, K.G.U. Wijayantha, S. Saremi-Yarahmadi, M. Mazhar, V. McKee, Nanostructured α-Fe_2O_3 thin films for photoelectrochemical hydrogen generation, Chem. Mater. 21 (2009) 3763–3772.
[9] A.A. Tahir, M. Mazhar, M. Hamid, K.G.U. Wijayantha, K.C. Molloy, Photooxidation of water by $NiTiO_3$ deposited from single source precursor $[Ni_2Ti_2(OEt)_2(\mu\text{-}OEt)_6(acac)_4]$ by AACVD, Dalton Trans. (2009) 3674–3680.
[10] V.R. Satsangi, S. Kumari, A.P. Singh, R. Shrivastav, S. Dass, Nanostructured hematite for photoelectrochemical generation of hydrogen, Int. J. Hydrogen Energy 33 (2008) 312–318.
[11] J.A. Glasscock, P.R.F. Barnes, I.C. Plumb, N. Savvides, Enhancement of photoelectrochemical hydrogen production from hematite thin films by the introduction of Ti and Si, J. Phys. Chem. C 111 (2007) 16477–16488.
[12] C.J. Sartoretti, B.D. Alexander, R. Solarska, I.A. Rutkowska, J. Augustynski, Photoelectrochemical oxidation of water at transparent ferric oxide film electrodes, J. Phys. Chem. B 109 (2005) 13685–13692.
[13] J. Qiu, C. Wang, M. Gu, Photocatalytic properties and optical absorption of zinc ferrite nanometer films, Mater. Sci. Eng. B 112 (2004) 1–4.
[14] M.A. Valenzuela, P. Bosch, J. Jimeĭnez-Becerrill, O. Quiroz, A.I. Páez, Preparation, characterization and photocatalytic activity of ZnO, Fe_2O_3 and $ZnFe_2O_4$, J. Photochem. Photobiol. A: Chem. 148 (2002) 177–182.
[15] P. Cheng, W. Li, T. Zhou, Y. Jin, M. Gu, Physical and photocatalytic properties of zinc ferrite doped titania under visible light irradiation, J. Photochem. Photobiol. A: Chem. 16 (2004) 97–101.
[16] Z.H. Yuan, L.D. Zhang, Synthesis, characterization and photocatalytic activity of $ZnFe_2O_4/TiO_2$ nanocomposite, J. Mater. Chem. 11 (2001) 1265–1268.
[17] J. Yin, L.-J. Bie, Z.-H. Yuan, Photoelectrochemical property of $ZnFe_2O_4/TiO_2$ double-layered films, Mater. Res. Bull. 42 (2007) 1402–1406.
[18] A.A. Tahir, K.G.U. Wijayantha, M. Mazhar, V. McKee, $ZnFe_2O_4$ thin films from a single source precursor by aerosol assisted chemical vapour deposition, Thin Solid Films 518 (2010) 3664–3668.
[19] G. Boschloo, D. Fitzmaurice, Spectroelectrochemistry of highly doped nanostructured tin dioxide electrodes, J. Phys. Chem. B 103 (1999) 3093–3098.
[20] C.M. Eggleston, A.J.A. Shankle, A.J. Moyer, I. Cesar, M. Grätzel, Anisotropic photocatalytic properties of hematite, Aquat. Sci. 71 (2009) 151–159.
[21] M. Maletin, E.G. Moshopoulou, A.G. Kontos, E. Devlin, A. Delimitis, V.T. Zaspalis, L. Nalbandian, V.V. Srdic, Synthesis and structural characterization of In-doped $ZnFe_2O_4$ nanoparticles, J. Eur. Ceram. Soc. 27 (2007) 4391–4394.
[22] Z. Wang, D. Schiferl, Y. Zhao, H.St.C. O'Neill, High pressure Raman spectroscopy of spinel-type ferrite $ZnFe_2O_4$, J. Phys. Chem. Solids 64 (2003) 2517–2523.
[23] M.L. Wen, Q. Li, Y.T. Li, Magnetic, electronic and structural properties of $Zn_xFe_{3-x}O_4$, J. Electron Spectrosc. Relat. Phenom. 153 (2006) 65–70.
[24] Y.N. Nuli, Y.Q. Chu, Q.Z. Qin, Nanocrystalline $ZnFe_2O_4$ and Ag-doped $ZnFe_2O_4$ films used as new anode materials for Li-ion batteries, J. Electrochem. Soc. 151 (2004) A1077–A1083.
[25] Y. Sharma, N. Sharma, G.V.S. Rao, B.V.R. Chowdari, Li-storage and cyclability of urea combustion derived $ZnFe_2O_4$ as anode for Li-ion batteries, Electrochim. Acta 53 (2008) 2380–2385.
[26] P. Druska, U. Steinike, V. Sepelak, Surface structure of mechanically activated and of mechanosynthesized zinc ferrite, J. Solid State Chem. 146 (1999) 13–21.
[27] G.C. Allen, S.J. Harris, J.A. Juston, A study of a number of mixed transition metal oxide spinels using X-ray photoelectron spectroscopy, Appl. Surf. Sci. 37 (1989) 111–134.
[28] Y.Q. Chu, Z.W. Fu, Q.Z. Qin, Cobalt ferrite thin films as anode material for lithium ion batteries, Electrochim. Acta 49 (2004) 4915–4921.
[29] K. Wandelt, Photoemission studies of adsorbed oxygen and oxide layers, Surf. Sci. Reports 2 (1982) 1–121.
[30] C. Santato, M. Odziemkowski, M. Ulmann, J. Augustynski, Crystallographically oriented mesoporous WO_3 films: synthesis, characterization, and applications, J. Am. Chem. Soc. 123 (2001) 10639–10649.
[31] S.U.M. Khan, J. Akikusa, Photoelectrochemical splitting of water at nanocrystalline *n*-Fe_2O_3 thin-film electrodes, J. Phys. Chem. B 103 (1999) 7184–7189.
[32] C. Piccirillo, R. Binions, I.P. Parkin, Synthesis and functional properties of vanadiun oxides: V_2O_3, VO_2 and V_2O_5 deposited on glass by aerosol-assisted CVD, Chem. Vap. Depos. 13 (2007) 145–151.
[33] X. Hou, K.-L. Choy, Processing and applications of aerosol-assisted chemical vapour deposition, Chem. Vap. Depos. 12 (2006) 583–596.
[34] L.M. Peter, K.G.U. Wijayantha, Electron transport and back reaction in dye sensitised nanocrystalline photovoltaic cells, Electrochim. Acta 45 (2000) 4543–4551.
[35] L.M. Peter, D. Vanmaekelbergh, in: R.C. Alkire, D.M. Kolb (Eds.), Advances in Electrochemical Science and Engineering, vol. 6, Wiley-Interscience, Chichester U.K, 1999, p. 77.
[36] S. Kumari, C. Tripathi, A.P. Singh, D. Chauhan, R. Shrivastav, S. Dass, V.R. Satsangi, Characterization of Zn-doped hematite thin films for photoelectrochemical splitting of water, Curr. Sci. 19 (2006) 1062–1064.
[37] S. Kumari, A.P. Singh, C. Tripathi, D. Chauhan, S. Dass, R. Shrivastav, V. Gupta, K. Sreenivas, V.R. Satsangi, Enhanced photoelectrochemical response of Zn-dotted hematite, Int. J. Photoenergy (2007) (Article ID 87467).
[38] W.B. Ingler Jr., J.P. Baltrus, S.U.M. Khan, Photoresponse of p-type zinc-doped iron(III) oxide thin films, J. Am. Chem. Soc. 126 (2004) 10238–10239.
[39] Z. Cvejić, S. Rakić, S. Jankov, S. Skuban, A. Kapor, Dielectric properties and conductivity of zinc ferrite and zinc ferrite doped with yttrium, J. Alloys Compd. 480 (2009) 241–245.